

# Photoluminescence Modulation of Graphene/MoS<sub>2</sub> Heterostructures Separated by Laser-Induced Functionalization

Qing Cao, Mira Krefler, Marleen Hußmann, Yalei Hu, Patryk Kusch, and Siegfried Eigler\*



Cite This: *Chem. Mater.* 2024, 36, 3267–3276



Read Online

ACCESS |



Metrics & More

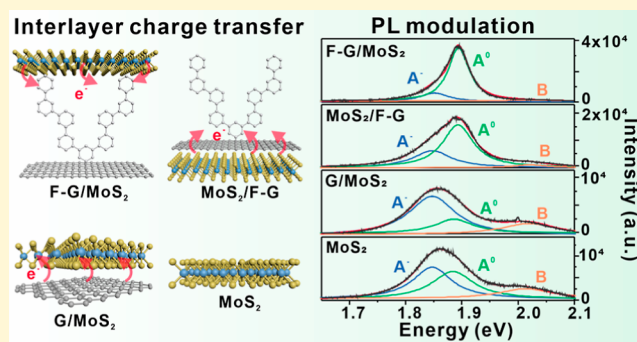


Article Recommendations



Supporting Information

**ABSTRACT:** Tuning the optoelectronic properties of monolayer MoS<sub>2</sub> (1L-MoS<sub>2</sub>) is highly desired for optoelectronic applications. Gaining profound insights into the fundamental mechanisms that govern optoelectronic properties is of utmost significance. Here, we demonstrate that the photoluminescence (PL) of 1L-MoS<sub>2</sub> can be modulated by photochemically functionalized graphene (F-G), which is covalently modified by oligophenyl groups. More importantly, the layer stacking sequence of F-G and 1L-MoS<sub>2</sub> brings different interface structures, resulting in a significant difference in the PL enhancement. MoS<sub>2</sub> supported by F-G (F-G/MoS<sub>2</sub>) has a 5-fold PL enhancement, while it only shows a 1.8-fold PL enhancement if stacked underneath F-G (MoS<sub>2</sub>/F-G). Accordingly, the results indicate that the oligophenyl groups in F-G/MoS<sub>2</sub> not only have a p-doping effect on MoS<sub>2</sub> but also largely prevent electron donation from the graphene basal plane with an enlarged interlayer distance of 8 nm. Consequently, the PL enhancement is lost with the thermal defunctionalization of F-G. Thus, we conclude that the functional groups can be considered as separate molecular components with the vertical arrangement in the functionalized heterostructure system. The photoactive graphene acts as a template for perpendicular molecular alignment in the heterointerface construction. The F-G/MoS<sub>2</sub> heterostructures bring new perspectives to the design and investigation of optoelectronic devices.



Two-dimensional transition-metal dichalcogenides (2DTMDs) monolayers have attracted massive research attention over the past decade due to their unique electronic, optical, and mechanical properties, which remarkably differ from the properties of their respective bulk materials.<sup>1–3</sup> As a prototypical 2DTMD, monolayer molybdenum disulfide (1L-MoS<sub>2</sub>) transforms from an indirect band gap (1.2 eV) semiconductor in its bulk form to a direct band gap (1.8 eV) semiconductor, owing to which photoluminescence (PL) emerges in 1L-MoS<sub>2</sub> with sensitive photo response.<sup>4,5</sup> Optically generated electron–hole pairs in 1L-MoS<sub>2</sub> form stable excitonic states due to large Coulomb interactions in atomically thin layers.<sup>6</sup> Many-body bound states, such as charged exciton (trion), can be formed through the interplay between an exciton and a charge carrier by tuning the electron densities in 1L-MoS<sub>2</sub>, thereby enabling variable PL properties to meet different optoelectronic applications, such as photo-detectors, photovoltaics, sensors, and light emitters.<sup>7</sup> Various approaches, including electrical gating,<sup>8</sup> chemical doping,<sup>6</sup> defect engineering,<sup>9</sup> covalent functionalization,<sup>10,11</sup> and plasma treatment,<sup>12</sup> have been employed to realize the PL enhancement or quenching of 1L-MoS<sub>2</sub>. Nevertheless, these approaches either require complicated methods, are sensitive to chemical contamination, or cause structural damage to the structure.<sup>9</sup>

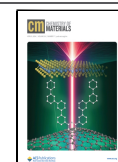
Stacking of 1L-MoS<sub>2</sub> with different 2D materials, such as graphene, hBN, or other TMDs by van der Waals forces, also makes the excitonic states of MoS<sub>2</sub> adjustable through quantum coupling.<sup>13,14</sup> Among which, graphene is a semimetal composed of sp<sup>2</sup>-hybridized carbon atoms in a honeycomb lattice array, exhibiting outstanding properties such as high carrier mobility up to 10<sup>5</sup> cm<sup>2</sup> V<sup>-1</sup> s<sup>-1</sup> at room temperature, quantum electronic transport, high optical transparency (~97.7%), and large tunability of the Fermi level.<sup>15–17</sup> These superiorities make it an ideal heterogeneous layer to change the excitonic states in MoS<sub>2</sub> via interlayer charge transfer. It is reported that the PL of 1L-MoS<sub>2</sub> becomes quenched when stacked with pristine graphene.<sup>18,19</sup> Due to the Schottky barrier at the interface, the photogenerated holes are injected from the valence band of MoS<sub>2</sub> to graphene, while the photogenerated electrons in the conduction band of MoS<sub>2</sub> are not allowed to diffuse to graphene.<sup>19,20</sup> Derivatives of graphene, such as

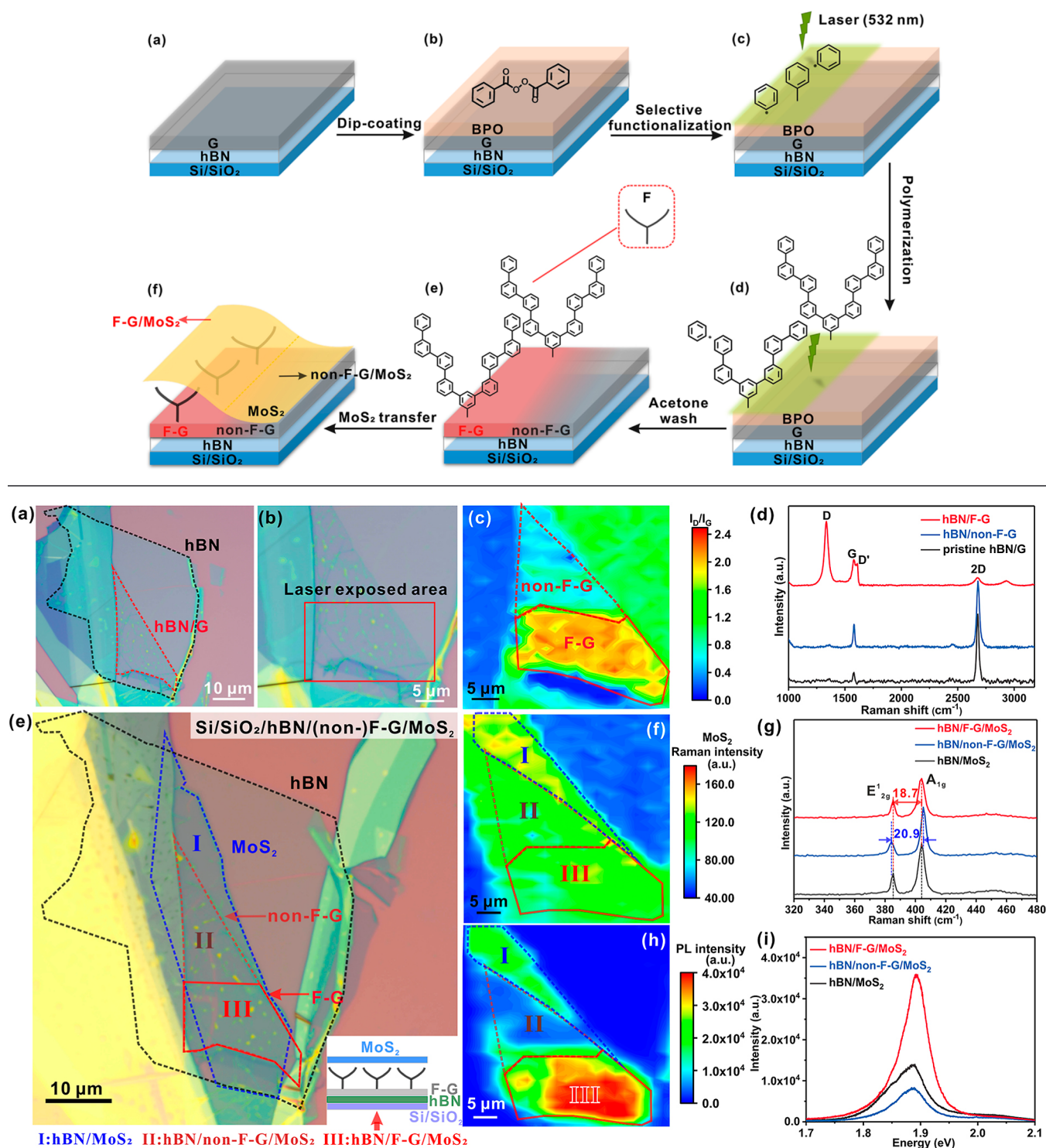
Received: December 13, 2023

Revised: January 25, 2024

Accepted: January 29, 2024

Published: February 16, 2024



Scheme 1. Schematic Illustration of the Laser-Induced Functionalization Process for Fabricating hBN/(non-)F-G/MoS<sub>2</sub> Heterostructure

**Figure 1.** (a) Optical microscopy images of the hBN/G heterostructure. (b) Laser-exposed area on hBN/G/BPO as marked in the red box. (c)  $I_D/I_G$  Raman mapping of hBN/G after functionalization. (d) Average Raman spectra of pristine hBN/G, hBN/non-F-G, and hBN/F-G. hBN/(non-)F-G/MoS<sub>2</sub> heterostructure. (e) Optical microscopy image, insert of (e) schematic structure of hBN/F-G/MoS<sub>2</sub>, (f) MoS<sub>2</sub> Raman intensity mapping, (g) MoS<sub>2</sub> Raman spectra, (h) MoS<sub>2</sub> PL intensity mapping, and (i) PL spectra.

graphene oxides (GO),<sup>21</sup> oxo-functionalized graphene (oxo-G),<sup>22</sup> reduced oxo-functionalized graphene (r-oxo-G),<sup>22</sup> and porous graphene,<sup>23</sup> have been used to enhance the PL intensity of 1L-MoS<sub>2</sub>. Owing to the rich electron-withdrawing groups in GO and oxo-G, such as hydroxyl, epoxy, and organosulfates, or

the defective sites in r-oxo-G and porous graphene, a p-doping effect with a PL enhancement of the neutral exciton is observed in 1L-MoS<sub>2</sub>.<sup>21–23</sup> In addition to the noncovalent heterostructures, Chen et al. fabricate a covalently linked MoS<sub>2</sub>/graphene heterostructure generating PL changes in 1L-

MoS<sub>2</sub>.<sup>11</sup> First, a 4-bromophenyl functionalized MoS<sub>2</sub> layer is prepared on a Si/SiO<sub>2</sub> substrate by reacting the generated negatively charged MoS<sub>2</sub> with 4-bromobenzenediazonium tetrafluoroborate. Subsequently, a graphene layer is transferred on top. Through the laser-triggered free radical reaction of 4-bromophenyl groups, the overlaying graphene is covalently attached from underneath to functionalized MoS<sub>2</sub>. However, the covalent heterostructure shows remarkable PL quenching, which is due to the efficient charge transfer at the covalently bonded interface. Structures like those require complex preparation processes, and the PL changes are considered as a result of charge transfer. However, 2D materials are not only sensitive to charge-transfer doping but also susceptible to interlayer interactions as they are atomically thin.<sup>24</sup> Interlayer van der Waals interactions and interlayer distance are very important factors but are rarely considered in studying the PL of graphene/MoS<sub>2</sub> heterostructures (G/MoS<sub>2</sub>).

Herein, we report on the effect of functional groups interacting with MoS<sub>2</sub> in the perpendicular orientation. PL modulation of 1L-MoS<sub>2</sub> is realized via the monotopic covalent photochemical functionalization of graphene in G/MoS<sub>2</sub> heterostructures. Through Raman, PL, dual scanning near-field optical microscopy (dual s-SNOM), and Kelvin probe force microscopy (KPFM), we identify the boundaries and the distinct characteristics of the selectively functionalized regions and the pristine regions on the heterostructures. In G/MoS<sub>2</sub>, the functionalized area of graphene (F-G/MoS<sub>2</sub>) exhibits a 5-fold enhancement in the PL intensity of MoS<sub>2</sub> compared to the nonfunctionalized area of graphene. Furthermore, the reverse stacked MoS<sub>2</sub>/F-G heterostructure is fabricated by in situ functionalizing MoS<sub>2</sub>/G/benzoyl peroxide (BPO) through photochemical reaction and only shows a 1.8-fold PL increase compared to pristine G/MoS<sub>2</sub>. This observation demonstrates the role of monotopic functionalization in differentiating surfaces of 2D materials. We conclude on the flexible role of F-G in the PL modulation of 1L-MoS<sub>2</sub>.

## RESULTS AND DISCUSSION

**Fabrication and Characterization of the hBN/(non-)F-G/MoS<sub>2</sub> Heterostructure.** To keep the explanation of heterostructures concise, herein, we define the vertical stacking order of the heterojunction layers as (substrate/)bottom layer/upper layer. As shown schematically in Scheme 1a and Figure 1a, few-layer hBN with a thickness of 6 nm (Figure S1) was exfoliated and transferred to a Si/SiO<sub>2</sub> (300 nm) wafer substrate. Then, a monolayer of graphene exfoliated from HOPG was transferred to the hBN flake (hBN/G). The hBN/G structure was subsequently annealed in vacuum at 150 °C for 2 h to remove water and organic residues originating from the transfer process.<sup>25</sup> The utilization of the hBN layer is to stabilize the flat structure of the graphene flake during repeated solution treatments because hBN has a superior flatness compared to Si/SiO<sub>2</sub>.<sup>26</sup> Then, a thin film of BPO was formed by dip-coating hBN/G to yield hBN/G/BPO (Scheme 1b). The photochemical functionalization of graphene was carried out by a 532 nm Raman laser treatment at a power of 1 mW. Under laser irradiation, the BPO decomposes to phenyl radicals and CO<sub>2</sub> by accepting a hot electron from photoexcited graphene. The phenyl radicals subsequently attack the basal plane of graphene (Scheme 1c).<sup>27</sup> Following the establishment of phenyl-functional sites on the basal plane, the phenyl radicals are likely to attack the bound phenyl groups, resulting in the formation of polymerized dendritic

structures (Scheme 1d).<sup>27–29</sup> To exclude any damaging effect from the laser energy input or in combination with solvent residues, we conducted reference experiments for pristine graphene and graphene treated with acetone. Therefore, the reference structures were treated for accumulated laser irradiation times from 1 to 300 s. According to the Raman spectra of nondefective graphene displayed in Figure S2, the graphene is stable under the used laser irradiation conditions and acetone treatment. For hBN/G/BPO, we find that the degree of functionalization of graphene is radiation time-dependent. Accordingly, with accumulated laser acquisition time from 1 to 50 s, the maximum functionalization density was indicated by the Raman spectra (Figure S3). Thus, for further experiments, we used 50 s irradiation time for the monotopic functionalization of hBN/G. By using the mapping function of the scanning Raman instrument, regioselective laser irradiation can be performed to illuminate only half of the graphene sheet, as marked by the green area in Scheme 1c and the red box in Figure 1b. After laser-induced functionalization, the residual BPO film was washed with acetone (Scheme 1e). The readout process of Raman spectra of the as-functionalized hBN/G was accomplished at a lower laser power of 0.5 mW and 1 s irradiation time. As can be seen in the I<sub>D</sub>/I<sub>G</sub> Raman intensity mapping in Figure 1c, the illuminated region can be clearly distinguished as a result of functionalization (F-G), unlike the rest of the graphene flake (non-F-G). The average Raman spectra of pristine hBN/G before functionalization, hBN/F-G, and hBN/non-F-G are depicted in Figure 1d, respectively. There are two dominant peaks in the Raman spectra of pristine hBN/G and hBN/non-F-G: G-band (at 1580 cm<sup>-1</sup>) and 2D-band (at 2680 cm<sup>-1</sup>). The absence of a D-band (at 1340 cm<sup>-1</sup>) indicates the defect-free graphene in hBN/G and hBN/non-F-G. For F-G, the D and D' peaks appear in the Raman spectra. A uniform functionalization with an average I<sub>D</sub>/I<sub>G</sub> of 2.2 is indicated, representing that the functionalization degree is around 1%.<sup>30</sup>

After functionalization of hBN/G, mechanically exfoliated 1L-MoS<sub>2</sub> was directly transferred on top of the hBN/G to form the areas of hBN/F-G/MoS<sub>2</sub> and hBN/non-F-G/MoS<sub>2</sub> (Scheme 1f and Figure 1e). Afterward, hBN/(non-)F-G/MoS<sub>2</sub> was annealed in vacuum at 200 °C for 2 h to enhance the interlayer contact since low-weight molecular contaminants are known to be eliminated from the interior.<sup>31</sup> As shown in Figure 1f, the Raman intensity of MoS<sub>2</sub> on hBN/(non-)F-G is uniform, although the MoS<sub>2</sub> Raman signal on hBN (hBN/MoS<sub>2</sub>), as marked in region I, is slightly increased owing to the electric neutral characteristic of hBN.<sup>32</sup> The Raman spectra of heterojunction areas display the typical vibration modes of 1L-MoS<sub>2</sub> and 1L-graphene, which indicates the effective formation of the heterostructure (Figure S4). The magnified Raman spectra of MoS<sub>2</sub> in the range of 300–500 cm<sup>-1</sup> are shown in Figure 1g. Two peaks, the in-plane E<sub>2g</sub><sup>1</sup> (385.4 cm<sup>-1</sup>) and the out-of-plane A<sub>1g</sub> (404.1 cm<sup>-1</sup>) appear in the Raman spectrum of the hBN/MoS<sub>2</sub> layer. The frequency difference between E<sub>2g</sub><sup>1</sup> and A<sub>1g</sub> is 18.7 cm<sup>-1</sup>, confirming the monolayer characteristic of the MoS<sub>2</sub> flake.<sup>6</sup> It has been reported that the A<sub>1g</sub> mode is sensitive to charge-doping and the E<sub>2g</sub><sup>1</sup> mode is sensitive to lattice distortions or strain in MoS<sub>2</sub>.<sup>33</sup>

The frequency difference between E<sub>2g</sub><sup>1</sup> and A<sub>1g</sub> in hBN/non-F-G/MoS<sub>2</sub> is 20.9 cm<sup>-1</sup>, which is 2.2 cm<sup>-1</sup> higher than the value of hBN/MoS<sub>2</sub> due to the electron donation from graphene to MoS<sub>2</sub>.<sup>33</sup> However, after the functionalization, the E<sub>2g</sub><sup>1</sup> and A<sub>1g</sub> modes in hBN/F-G/MoS<sub>2</sub> with a difference of 18.7

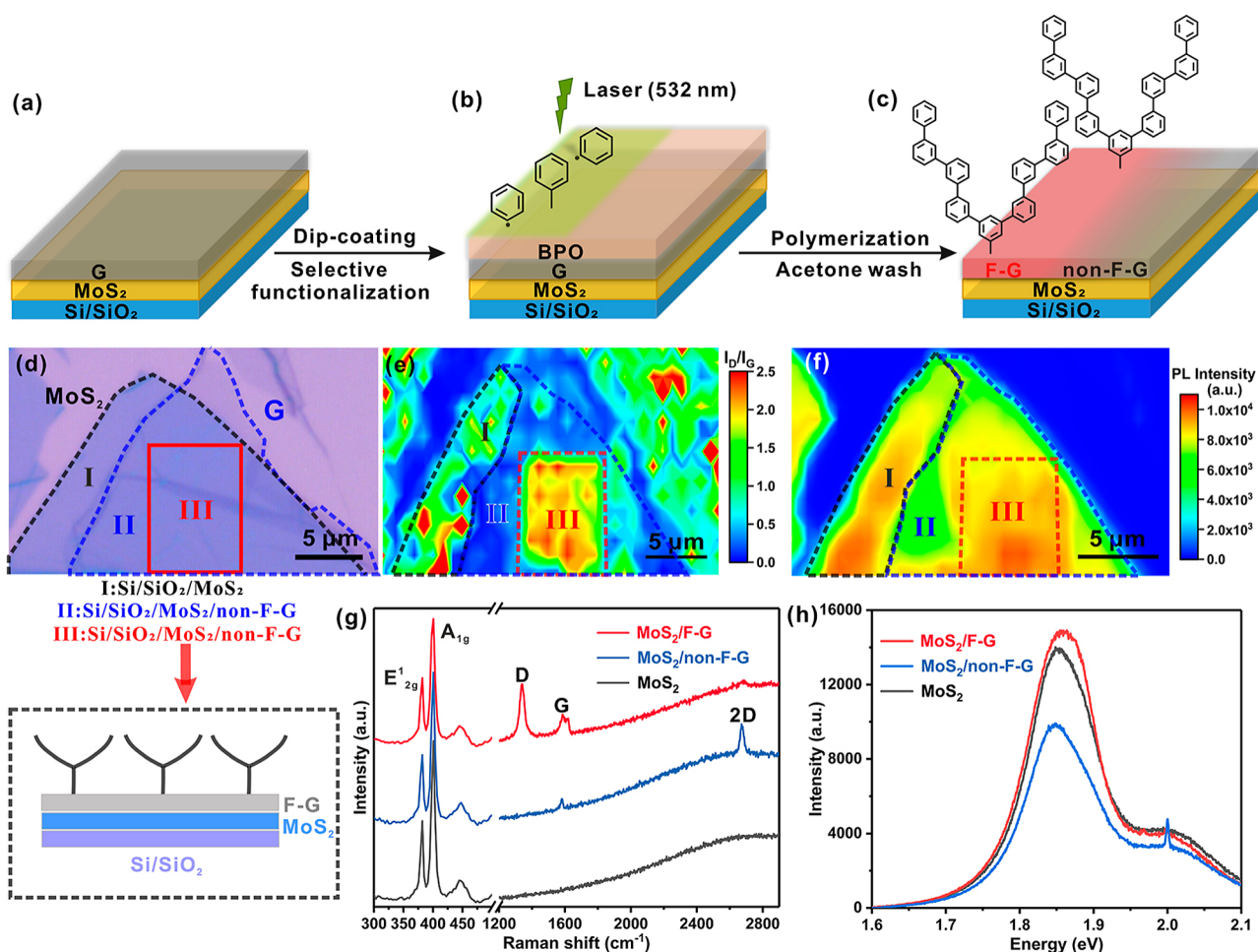


**Figure 2.** MoS<sub>2</sub>/(non-)F-G heterostructure: (a–c) schematic illustration of the process for fabrication. (d) Optical microscopy image and schematic structure, (e)  $I_D/I_G$  Raman intensity mapping, (f) MoS<sub>2</sub> PL intensity mapping, (g) Raman spectra, and (h) PL spectra.

$\text{cm}^{-1}$  have no obvious shift compared to the hBN/MoS<sub>2</sub>. We deduce that there are two possible reasons: on the one hand, the weak electron-withdrawing effect from the oligophenyl groups cannot generate a large shift of the A<sub>1g</sub> Raman mode of MoS<sub>2</sub>. On the other hand, the oligophenyl functional groups effectively separate the graphene basal plane and MoS<sub>2</sub> interface with an increased interlayer distance, which impairs the electron transfer from the carbon plane to MoS<sub>2</sub>. The MoS<sub>2</sub> in hBN/F-G/MoS<sub>2</sub> is mainly supported by the phenyl groups instead of the graphene surface, resulting in partly free-standing MoS<sub>2</sub>. Figure 1h depicts the MoS<sub>2</sub> PL intensity mapping of the hBN/(non-)F-G/MoS<sub>2</sub> heterostructure. The F-G with a high  $I_D/I_G$  shows an enhanced PL intensity of MoS<sub>2</sub> (region III), which is 5 times and 3 times increased compared to hBN/non-F-G/MoS<sub>2</sub> (region II) and hBN/MoS<sub>2</sub> (region I), respectively. The PL maximum of the hBN/F-G/MoS<sub>2</sub> structure (1.89 eV) is red-shifted by 0.01 eV compared to hBN/non-F-G/MoS<sub>2</sub> and hBN/MoS<sub>2</sub> (1.88 eV), respectively, due to the p-doping effect of the phenyl groups (Figure 1i). In addition, laser-induced effects can be excluded, since the laser radiation did not generate PL changes for pristine MoS<sub>2</sub> and MoS<sub>2</sub>/G, respectively (Figures S5a and S6). Moreover, the potential BPO residues on the surface cannot vary the PL properties of MoS<sub>2</sub> under the operational laser energy, as reference experiments revealed (Figure S5b). The profile maps corresponding to Figure 1c,f,h are displayed in Figure S7. The frequency distribution centers are consistent with the different

intervals on the relevant mapping images. In addition, since the PL intensity of MoS<sub>2</sub> is sensitive to the variations in samples, such as bubbles, strain, contamination, and measurement environment, several (hBN)/(non-)F-G/MoS<sub>2</sub> samples have been prepared, as shown in Figure S8, demonstrating the reproducibility of fabrication and measured properties. Based on the results, it is confirmed that the F-G layer significantly enhances the PL of MoS<sub>2</sub>.

**Fabrication and Characterization of the MoS<sub>2</sub>/(non-)F-G Heterostructure.** Compared to the electron-withdrawing groups in GO, such as hydroxyl, epoxy, and organosulfates,<sup>34,35</sup> the phenyl groups have a very weak electron-withdrawing effect. Nevertheless, the F-G/MoS<sub>2</sub> shows comparable PL enhancement for MoS<sub>2</sub> to that of GO/MoS<sub>2</sub>, as we reported in previous works,<sup>21,22</sup> demonstrating that the electronic effect of the functional groups is not the only factor in the PL enhancement of MoS<sub>2</sub>. To elucidate further effects, a reversely stacked MoS<sub>2</sub>/F-G heterostructure was fabricated. The F-G placed on top of MoS<sub>2</sub> can keep the electron-withdrawing effect induced by the oligophenyl groups, but it has better interlayer contact with the graphene lattice compared to the F-G/MoS<sub>2</sub>. Figure 2a–c illustrates the fabrication process of the MoS<sub>2</sub>/F-G heterostructure. First, a mechanically exfoliated 1L-MoS<sub>2</sub> was transferred onto a Si/SiO<sub>2</sub> (300 nm) wafer. Then, a monolayer of graphene was transferred to the 1L-MoS<sub>2</sub> to form a MoS<sub>2</sub>/G heterostructure. The MoS<sub>2</sub>/G heterostructure was annealed in vacuum at 200

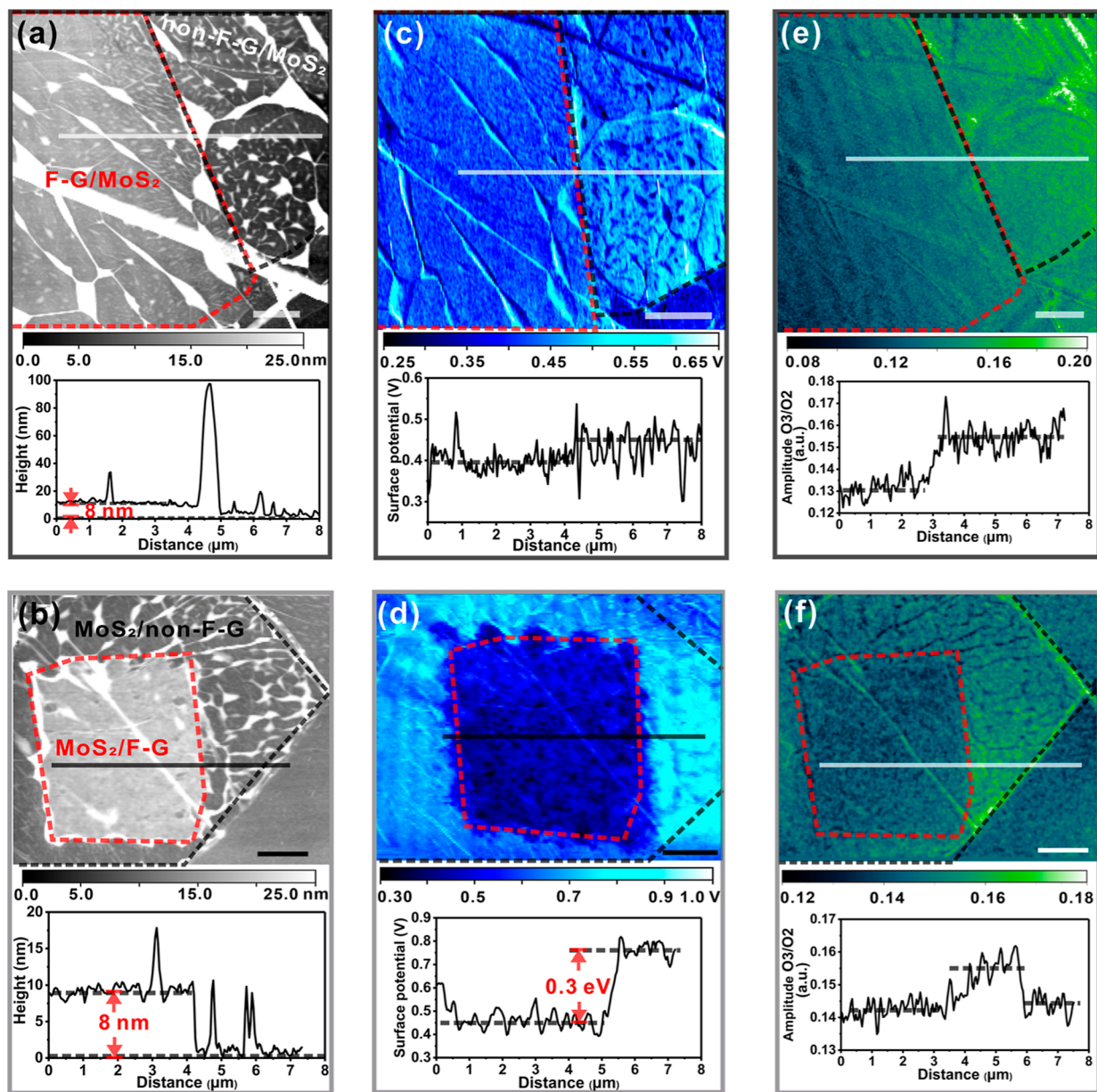


**Figure 3.** (a,b) AFM topography together with (c,d) KPFM images and (e,f) s-SNOM images at the same sample area for (non-)F-G/MoS<sub>2</sub> and MoS<sub>2</sub>/(non-)F-G, respectively. The scale bars in (a–f) are 5 μm.

°C for 2 h, and then a thin layer of BPO was deposited on the graphene surface of the heterostructure by dip-coating (5 mM, in acetone) to fabricate MoS<sub>2</sub>/G/BPO. The laser functionalization process is identical to the previously described procedure for the functionalization of hBN/G/BPO (Scheme 1b–e). However, here, in situ functionalization is directly carried out on the surface of the MoS<sub>2</sub>/G heterostructure without further transfer process compared to F-G/MoS<sub>2</sub>. The laser irradiation area on MoS<sub>2</sub>/G is marked by the green area in Figure 2b and the red box (region III), as shown in the optical microscopy image (Figure 2d). After 50 s of laser exposure and acetone washing, the functionalized area on MoS<sub>2</sub>/G (MoS<sub>2</sub>/F-G) marked as region III shows a high  $I_D/I_G$  intensity of around 2.2 (Figure 2e) with a slight increase in the PL intensity of MoS<sub>2</sub> (Figure 2f). In contrast, the non-functionalized area of MoS<sub>2</sub>/G (MoS<sub>2</sub>/non-F-G) marked as region II shows PL quenching of MoS<sub>2</sub>. In Figure 2g, the average Raman spectra of MoS<sub>2</sub>/F-G (region III), MoS<sub>2</sub>/non-

F-G (region II), and isolated MoS<sub>2</sub> (region I) from the three different areas on the MoS<sub>2</sub>/G heterostructure are shown. The  $E_{2g}^1$  (385.4 cm<sup>-1</sup>) and  $A_{1g}$  (404.1 cm<sup>-1</sup>) peaks in the Raman spectrum of the isolated 1L-MoS<sub>2</sub> layer confirm the monolayer character of the MoS<sub>2</sub> flake. Vibrational modes of both 1L-MoS<sub>2</sub> and 1L-graphene appear in the Raman spectra of the MoS<sub>2</sub>/F-G and MoS<sub>2</sub>/non-F-G regions, indicating the formation of heterostructures. The D peak appears in MoS<sub>2</sub>/F-G after functionalization with the attenuation of the 2D peak, and the degree of functionalization is around 1%, which is consistent with that of hBN/F-G/MoS<sub>2</sub> (Figure 1c). However, as the PL spectra in Figure 2h reveal, the PL intensity of MoS<sub>2</sub> only increases marginally by 1.1 and 1.8 times in comparison with isolated MoS<sub>2</sub> and MoS<sub>2</sub>/non-F-G, respectively. Owing to the p-doping effect induced by F-G, the PL maximum of MoS<sub>2</sub>/F-G shows a redshift compared with the pristine MoS<sub>2</sub>, however, the MoS<sub>2</sub>/F-G displays much lower PL enhancement than hBN/F-G/MoS<sub>2</sub>.

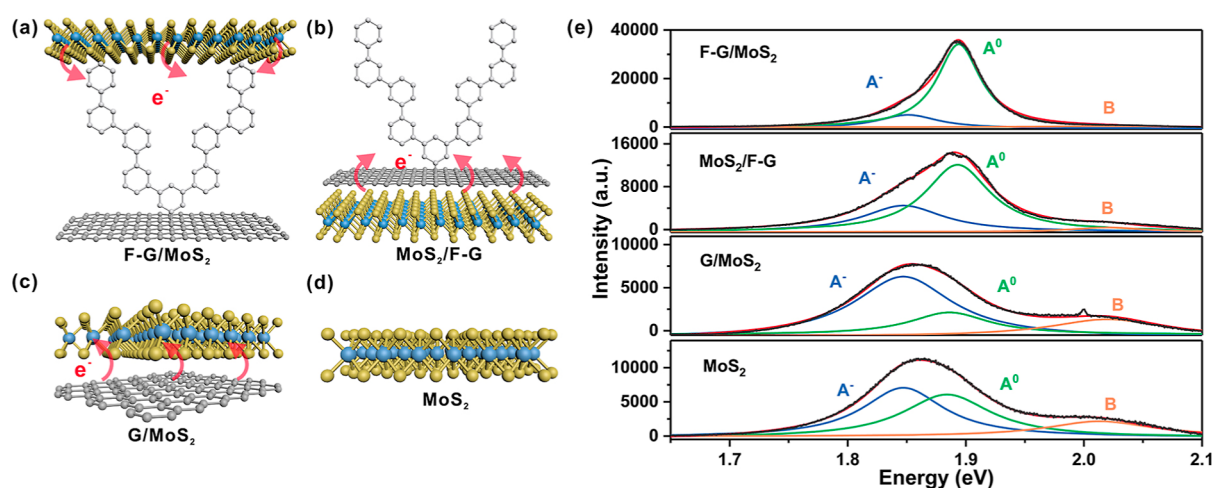


**Figure 4.** Sketch illustrating the interfacial interaction mechanism in the four heterostructures: (a) F-G/MoS<sub>2</sub>, (b) MoS<sub>2</sub>/F-G, (c) G/MoS<sub>2</sub>, and (d) MoS<sub>2</sub>. (e) Peak fittings using Lorentz functions for the four structures.

**Effect of Functionalization on the Dielectric Function and Surface Potential.** One way to accurately describe the electrical and optical features of nanoscale materials is to analyze their complex dielectric function, which is a measure of the transmission and absorption of light through a material as a function of frequency.<sup>36</sup> By employing Raman/PL spectroscopy, we investigated the effect of the functionalized groups on the photoelectric characteristics of G/MoS<sub>2</sub> heterostructures. However, the spatial resolution of these techniques is bound by the diffraction limit of light and does not provide information on the homogeneity of the prepared samples on the nanometer scale. Here, we use the dual *s*-SNOM as an advanced tool for nanoimaging that combines near-field optical microscopy, KPFM, Raman, and PL spectroscopy, enabling to spatially resolve the variation of the dielectric function and the surface work function with nanometer-scale resolution. In detail, to begin with, we measured the KPFM of the (non-)F-G/MoS<sub>2</sub> and MoS<sub>2</sub>/(non-)F-G. In KPFM, we determine a topography image by the AFM together with the surface work function as a function of tip position that varies, for example, with doping levels. Consequently, the sample height, surface roughness, boundaries, and charge transfer influence on the surface work function can be characterized. As depicted in the AFM images in Figure 3a,b, F-G regions on both (non-)F-G/MoS<sub>2</sub> and MoS<sub>2</sub>/(non-)F-G exhibit an 8 nm height difference compared with the non-F-G regions. The thickness is induced by the functional component, which further proves our speculation described in Scheme 1 that photochemical functionalization leads to the formation of polymerized or oligomerized phenyl chain structures. In addition, the functionalized areas display flatter surfaces with fewer wrinkles and bubbles compared to the nonfunctionalized areas of the heterostructures, which proves the homogeneity of the functionalization. We suppose that the dendritic functional structures support the surface of the sample away from the bubbles and contaminations introduced by the transfer process. Consistent with the AFM images, on both heterostructures, the functionalized region exhibits darker KPFM contrast (lower surface potential) than the non-functionalized region (Figure 3c,d), which can be ascribed to the anchoring of electron-withdrawing phenyl groups.<sup>37,38</sup> The detection of functionalization on the surface of MoS<sub>2</sub>/F-G is more feasible using KPFM, as it is a surface-sensitive method

that exclusively probes the surface and near-surface areas. There is a significant variation of 0.3 V in surface potential between MoS<sub>2</sub>/F-G and MoS<sub>2</sub>/non-F-G. The KPFM images are in perfect agreement with our input selective functionalization patterns as well as the respective MoS<sub>2</sub> PL mappings, as shown in Figure S9 [(non-)F-G/MoS<sub>2</sub>] and Figure 2d–f [MoS<sub>2</sub>/(non-)F-G].

To support the data, we take near-field images by *s*-SNOM. The detected signal is related to the tip–sample distance and the dielectric function. In the *s*-SNOM, the tip–sample distance is kept the same during the scan. Indeed, wrinkles and bubbles may influence and vary slightly the tip–sample distance; however, on flat areas, it is around held at 1 nm. Thus, strong changes in the near-field contrast are a result of changing dielectric function due to doping, straining, and defects. We find that the *s*-SNOM images are in excellent agreement with the KPFM. As indicated in Figure 3e,f, all the previously identified features can be identified in the *s*-SNOM images. Despite the influence of wrinkles and bubbles on the *s*-SNOM images, there is a distinct and uniform contrast from the F-G to non-F-G heterostructures for both (non-)F-G/MoS<sub>2</sub> and MoS<sub>2</sub>/(non-)F-G. The functionalization leads to doping and thus to an increase in the dielectric function. In addition, *s*-SNOM images of the pristine MoS<sub>2</sub> and G/MoS<sub>2</sub> structures are shown in Figure S10. Monolayer and bilayer MoS<sub>2</sub>, as well as different regions of G/MoS<sub>2</sub>, show clear near-field contrast arising from variations in the local dielectric value. Therefore, based on the KPFM and *s*-SNOM findings, we prove that the PL enhancements of MoS<sub>2</sub> are attributed to the photofunctionalization of graphene rather than any external factors like contaminants or bubbles.

**Electron Transfer in Heterostructures.** The differentiated PL characteristics of F-G/MoS<sub>2</sub> and MoS<sub>2</sub>/F-G prove that the structural disparity notably affects the PL of MoS<sub>2</sub>. Normalized average PL spectra extracted from the four different structures of F-G/MoS<sub>2</sub>, MoS<sub>2</sub>/F-G, G/MoS<sub>2</sub>, and pristine 1L-MoS<sub>2</sub> on Si/SiO<sub>2</sub> were compared (Figure S11). Corresponding statistics of PL map profiles and mapping are listed in Figure S12. To gain a better understanding of the spectral changes, peaks were fitted using Lorentzian functions. Corresponding to the three typical excitonic states of neutral exciton (A<sup>0</sup>, 1.89 eV), negatively charged trion (A<sup>-</sup>, 1.85 eV), and B exciton (2.02 eV), the PL spectra of F-G/MoS<sub>2</sub>, MoS<sub>2</sub>/

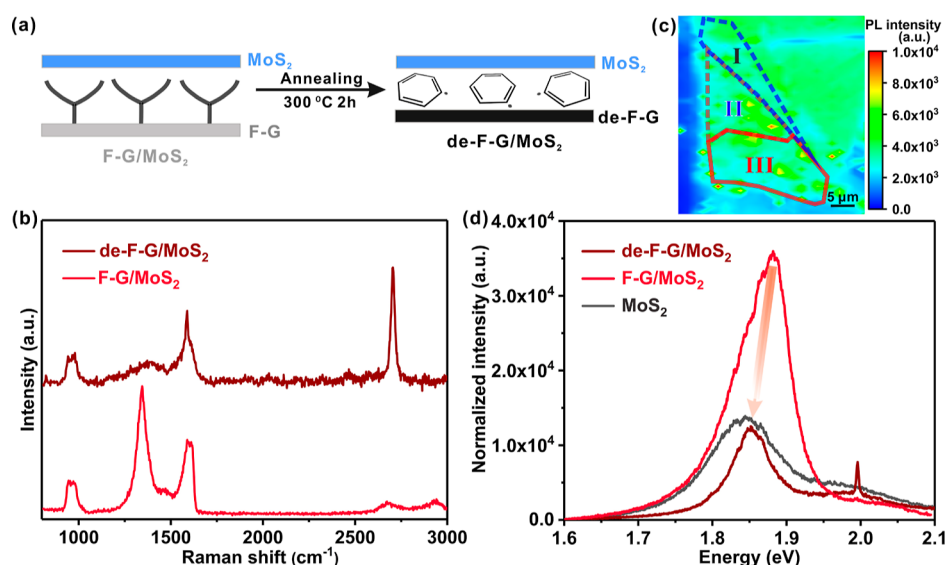


**Figure 5.** Defunctionalization of the hBN/(non-)F-G/MoS<sub>2</sub> heterostructure. (a) Schematic illustration of the defunctionalization process. (b) Raman spectra of F-G/MoS<sub>2</sub> and de-F-G/MoS<sub>2</sub>, (c) MoS<sub>2</sub> PL mapping image of the de-F-G/MoS<sub>2</sub> heterostructure, and (d) normalized PL spectra of de-F-G/MoS<sub>2</sub>, F-G/MoS<sub>2</sub>, and pristine MoS<sub>2</sub>.

F-G, G/MoS<sub>2</sub>, and MoS<sub>2</sub> were fitted by three Lorentzian functions (Figure 4e). Detailed parameters of fitted PL peaks by Lorentz functions are summarized in Table S1. In pristine 1L-MoS<sub>2</sub>, the PL spectrum is dominated by the trion state, which arises from reduced dielectric screening in gapped 2D crystals and the relatively heavy particle band masses associated with the Mo *d*-manifolds.<sup>8</sup> In contrast to pristine MoS<sub>2</sub>, the A<sup>-</sup> peak increases in G/MoS<sub>2</sub> and the A<sup>0</sup> peak is obviously weakened. Conversely, the A<sup>0</sup> excitons are the dominant contributors in the PL emission, with a 1.8-fold enhancement in MoS<sub>2</sub>/F-G and a 5-fold enhancement in F-G/MoS<sub>2</sub> compared to isolated MoS<sub>2</sub>, which indicates charge transfer from MoS<sub>2</sub> to F-G. The A<sup>0</sup> exciton peak intensity in F-G/MoS<sub>2</sub> is 11 times higher than that in G/MoS<sub>2</sub>. The additional peak at 2.0 eV in the PL spectrum of G/MoS<sub>2</sub> corresponds to the sharp 2D peak of monolayer graphene, which vanished in the PL spectra of F-G/MoS<sub>2</sub> and MoS<sub>2</sub>/F-G because of the functionalization of graphene. Figure 4a–c illustrates the electron transfer from MoS<sub>2</sub> to F-G for F-G/MoS<sub>2</sub> and MoS<sub>2</sub>/F-G. For G/MoS<sub>2</sub>, pristine graphene donates electrons to MoS<sub>2</sub>. Even though F-G shows electron-withdrawing ability, there is a significant difference in the effect on enhancing the PL of MoS<sub>2</sub> whether it is placed on top or under MoS<sub>2</sub>. This result indicates that the p-doping is not the only reason for the PL increase of MoS<sub>2</sub>. In F-G/MoS<sub>2</sub>, the MoS<sub>2</sub> is supported directly by the oligophenyl groups due to the high functionalization degree on the graphene surface, which increases the interlayer distance and decreases the van der Waals interaction between the graphene basal plane and MoS<sub>2</sub>. Compared to G/MoS<sub>2</sub>, there is no interlayer contact possible between MoS<sub>2</sub> and the graphene basal plane of F-G/MoS<sub>2</sub>, hindering also the electron transfer from the carbon plane to MoS<sub>2</sub> and consequently enhancing the PL intensity.

**Thermal Defunctionalization of the hBN/(non-)F-G/MoS<sub>2</sub> Heterostructure.** Moreover, the reversibility of the functionalization effect on the PL enhancement of MoS<sub>2</sub> is investigated. The hBN/(non-)F-G/MoS<sub>2</sub> heterostructure was annealed at 300 °C for 2 h in a vacuum to break the C-Aryl bond for restoring graphene (Figure 5a). As shown in the

Raman spectra in Figure 5b, the Raman signal of de-F-G recovers the narrow and most intense 2D peak. The sharp D peak vanishes, although a broad peak remains, most likely resulting from trapped dissociated polyphenyl or oligophenyl groups between graphene and MoS<sub>2</sub>. The 8 nm height resulting from the oligophenyl structures (Figure 3a) is largely reduced to about 0.8 nm after annealing, as depicted in Figure S13.

Accordingly, the PL enhancement from F-G also disappears after defunctionalization (Figure 5c,d). The PL intensity of de-F-G/MoS<sub>2</sub> is slightly lower than that of the isolated MoS<sub>2</sub> area because of the interlayer Schottky barrier. Compared to the vanished 2D peak of F-G/MoS<sub>2</sub>, the appearance of the 2D peak after annealing indicates the defunctionalization and restoration of graphene. However, the maximum of the PL peak of de-F-G/MoS<sub>2</sub> is red-shifted on account of the decoupled phenyl groups (Figure 5c). The absence of LA(M) peak at 227 cm<sup>-1</sup> in the MoS<sub>2</sub> Raman spectra (Figure S14) indicates that the annealing process in vacuum (1 × 10<sup>-3</sup> mbar) does not generate defects to MoS<sub>2</sub>. The loss of PL enhancement is mainly because of the annealing process, which breaks the covalent bonds of the oligophenyl groups oriented perpendicular to the graphene plane, leading to the free orientation of the dissociated oligophenyl groups.

## CONCLUSIONS

The PL of 1L-MoS<sub>2</sub> is demonstrated to be tunable by laser-induced oligophenyl-functionalized graphene. The s-SNOM, combined with AFM, KPFM, and Raman, allows us to characterize and understand the fabricated heterostructures. The monotopic functionalized graphene stacked on top or bottom of MoS<sub>2</sub> differentiates the heterointerface between graphene and MoS<sub>2</sub>, thus generating varied PL modulation. In addition, the MoS<sub>2</sub> supported on top of F-G results in significant increases of dominant A<sup>0</sup> excitons compared to the MoS<sub>2</sub> with direct interlayer interaction to the graphene basal plane (pristine G/MoS<sub>2</sub> and MoS<sub>2</sub>/F-G). The results indicate that the enlarged interlayer distance by the oligophenyl groups hinders the electron transfer from the graphene carbon plane

to MoS<sub>2</sub>. Moreover, the PL enhancement of MoS<sub>2</sub> is lost by thermally induced defunctionalization with the restoration of interlayer distances. Our findings prove that the interface designed by functional components and the accompanied tailoring of the interlayer distance of heterostructures provide major effects on the PL modulations. The graphene carbon plane acts as an active reaction template for the covalent attachment of perpendicular molecules, thus opening more possibilities for the fabrication of heterointerfaces. With that knowledge in mind, we change our way of thinking about functionalized 2D heterostructures.

## EXPERIMENTAL SECTION/METHODS

**Materials.** Si wafers with a 300 nm thick SiO<sub>2</sub> layer were purchased from the Fraunhofer Institut für Integrierte Systeme und Bauelementetechnologie IISB in Erlangen. BPO and acetone (HPLC) were purchased from Sigma-Aldrich Co. (Germany) and used without further treatment. Polydimethylsiloxane (PDMS) was purchased from Gel-Pack.

**Characterization.** Optical imaging and transfer processes were performed using a Nikon LV100ND microscope equipped with a self-built transfer stage.<sup>39</sup> Raman and PL characterizations were conducted using a confocal Raman microscope (Horiba Explorer, 532 nm excitation wavelength, 0.7 μm laser spot, 1200/2400 gratings, 0.5 and 1 mW, 100× objectives) in air. The 1 mW laser power was used for the functionalization process. The 2400 gratings were used for precise Raman characterization of MoS<sub>2</sub>. The general readout of Raman and PL maps was carried out by 1200 gratings and 0.5 mW power. AFM images were recorded on a JPK Nanowizard 4 equipped with NSG10/Au probes using a Tap300-G AFM probe, and intermittent contact mode was chosen. Annealing of the samples was carried out using a tube furnace (Nabertherm GmbH, 30–3000 °C).

For the s-SNOM and KPFM, we used the neaSNOM from neaSPEC, which is coupled to a fully tunable visible laser (Hübner). The neaSNOM provides near-field imaging, KPFM, and AFM. In s-SNOM, a metallic tip is illuminated by light, and plasmons are generated that promote a near-field between the tip and sample. The near-field enhances both the incoming and backscattered light by a factor  $f$  and is detected by a single-line CCD. The enhancement factor  $f$  is given by the tip-sample distance and the dielectric function of the sample. By scanning the tip across the sample and measuring the near-field signal as a function of it, the optical properties of the sample can be studied qualitatively. To achieve background suppression, the tip was oscillated with an amplitude of 50 nm and a frequency  $\Omega$  of approximately 250 kHz. The resulting signal was demodulated using the higher harmonics of the tip frequency  $n\Omega$ . To further reduce noise, a pseudoheterodyne interferometer was employed, which utilized a reference mirror oscillating at a much lower frequency  $M \ll \Omega$ . This caused the length of the reference beam path to change, leading to interference with the scattered signal. As a result, sidebands were generated around the fundamental harmonics at frequencies equal to plus or minus an integer multiplied by the reference frequency  $f = n\Omega + m M$ . In this detection method, both the amplitude and phase information were recorded from the sample, resulting in near-field amplitude and phase images at different sidebands of the fundamental harmonic. Increasing the sideband index, ( $m$ ), contributed to a reduction in noise present in the s-SNOM images. The dual s-SNOM technique was used to characterize the sample, employing a commercial s-SNOM (NeaSNOM from Neaspec GmbH, Germany). The platinum–iridium-coated AFM tips (23 nm coating thickness) from NanoWorld were used, featuring a tip apex radius of less than 25 nm. To excite the sample, a wavelength-tunable cw laser (Hübner C-Wave, 450–650 nm wavelength) was used, and it was guided through a beam expander onto a parabolic mirror with a high NA of 0.7. The parabolic mirror collects the backscattered light, and the laser light is focused onto the AFM tip, which then acts as a near-field probe in the visible spectral range. The

laser power used for all s-SNOM image measurements was approximately 1 mW at the tip, with an integration time of 16 ms. The tip amplitude was 53.5 nm, with a tapping frequency of 243 kHz. The neaSNOM also can measure the surface potential by KPFM. For KPFM, we used the Pt–Ir-coated Si tips (ACCESS-EFM probes, AppNano,  $k = 2.7 \text{ N m}^{-1}$ ). AM-KPFM was operated, which is sensitive to electrostatic force. The work function of the samples ( $\Phi_{\text{sample}}$ ) is defined by the following formula,  $\Phi_{\text{sample}} = q V_{\text{CPD}} + \Phi_{\text{tip}}$ , where  $V_{\text{CPD}}$  is the contact potential difference measured by the KPFM,  $\Phi_{\text{tip}}$  is the work function of the tip, and  $q$  is the elementary charge. The potential profile is measured by maintaining a constant distance of 50 nm between the tip and the sample surface.

**Fabrication of Heterostructures.** *Preparation of the hBN/G Heterostructure.* Few-layer hBN was mechanically exfoliated from bulk hBN via PDMS and transferred onto a Si/SiO<sub>2</sub> wafer. Monolayer graphene was mechanically exfoliated from HOPG via PDMS and transferred to the few-layer hBN flake. According to the transfer method reported previously, the transfer process was carried out under a microscope equipped with a self-built transfer stage.<sup>39</sup> The thicknesses of the exfoliated hBN and graphene were determined by optical contrast, Raman spectroscopy, and AFM. After every transfer step, the sample was mildly annealed in vacuum ( $10^{-3}$  mbar) at 150 °C for 2 h to remove water and residuals stemming from the transfer process.

*Photochemical Reaction of BPO on the hBN/G Heterostructure.* First, a 5 mM BPO solution in acetone was prepared. The wafer with the hBN/G sample was vertically held by a clean tweezer and slowly dipped in the BPO solution for 2 s and then carefully moved out and deposited on a glass slide. Within 5 min, the acetone evaporated under ambient conditions, and an optically uniform thin film of BPO formed on top of the hBN/G structure. A photochemical reaction was initiated by the 532 nm green Raman laser with a spot size of 0.7 μm and 1 mW energy. The selective functionalization on hBN/G was realized using the point-by-point mapping function of the scanning Raman instrument with incremental steps of 0.7 μm. The irradiation time of every point was calculated accumulatively. The laser illuminated the bottom half part of the graphene flake by defining a rectangular map of 20 μm × 15 μm. The illumination time at every step was 10 s, and the mapping was repeated five times so that the total illumination time accumulated to 50 s. After laser functionalization, the residual BPO molecule film was removed by acetone washing. The Raman spectra of the whole hBN/G structure were measured by a mapping function using an increment of 0.7 μm at 532 nm laser excitation with 1 s irradiation time at a lower energy of 0.5 mW, and other parameters remained the same.

*Preparation of the hBN/(non)-F-G/MoS<sub>2</sub> Heterostructure.* Monolayers of MoS<sub>2</sub> were mechanically exfoliated, and a single-layer flake was selected (identified by optical contrast and Raman spectroscopy, 18.7 cm<sup>-1</sup> wavenumber difference of A<sub>1g</sub>–E<sub>2g</sub><sup>1</sup>) and transferred to the as-prepared hBN/G via PDMS, covering both the functionalized area (F-G) and the nonfunctionalized area of graphene (non-F-G). The heterostructure was annealed at 200 °C for 2 h in vacuum ( $10^{-3}$  mbar) to enhance the interlayer contact between MoS<sub>2</sub> and hBN/G. The PL and Raman measurements were performed afterward. F-G/MoS<sub>2</sub> heterostructure was also fabricated directly on a Si/SiO<sub>2</sub> wafer without hBN for comparison studies. For determining the Raman shifts of MoS<sub>2</sub>, the 2400 grating was used.

*Preparation of the MoS<sub>2</sub>/F-G Heterostructure.* Exfoliated 1L-MoS<sub>2</sub> was transferred onto a Si/SiO<sub>2</sub> wafer, followed by a monolayer of graphene (MoS<sub>2</sub>/G). Then, the whole wafer with the MoS<sub>2</sub>/G heterostructure was dip-coated with a thin BPO layer (compare section “Photochemical Reaction of BPO on the hBN/G Heterostructure”). The laser-induced functionalization was carried out on the top of the upper graphene layer using the same parameters as for the preparation of F-G/MoS<sub>2</sub>.

*Defunctionalization Studies.* The heterostructures were annealed in a vacuum ( $10^{-3}$  mbar) at 300 °C for 2 h with a heating rate of 2 °C/min. The total processing time, including cooling to ambient, was 9 h.

## ■ ASSOCIATED CONTENT

## SI Supporting Information

The Supporting Information is available free of charge at <https://pubs.acs.org/doi/10.1021/acs.chemmater.3c03166>.

AFM image of the hBN/G heterostructure; stability test of graphene under laser irradiation and acetone solvent; Raman spectra of G/BPO after an accumulated laser irradiation time; Raman spectra of the hBN/(non-)F-G/MoS<sub>2</sub> heterostructure; PL spectra of pristine MoS<sub>2</sub> and MoS<sub>2</sub>/BPO after accumulated laser irradiation; PL spectra of G/MoS<sub>2</sub> after accumulated laser irradiation; Raman, PL map profiles, and corresponding intensity frequency distribution; reproducibility of the heterostructure and PL enhancement; functionalization of hBN/G/BPO and PL enhancement of hBN/(non-)F-G/MoS<sub>2</sub>; optical microscopy, AFM, and s-SNOM images of Si/SiO<sub>2</sub>/MoS<sub>2</sub> and G/MoS<sub>2</sub> heterostructures; comparison of PL spectra of different structures; PL map profile and mapping of different heterostructures on Si/SiO<sub>2</sub> wafers; AFM and PL mapping of hBN/(non-)F-G/MoS<sub>2</sub> after annealing; Raman spectra of MoS<sub>2</sub> over the de-F-G/MoS<sub>2</sub> heterostructure; and parameters about fitted PL peaks by the Lorentz function (PDF)

## ■ AUTHOR INFORMATION

## Corresponding Author

Siegfried Eigler – Institute of Chemistry and Biochemistry, Freie Universität Berlin, 14195 Berlin, Germany; [orcid.org/0000-0002-0536-8256](https://orcid.org/0000-0002-0536-8256); Email: [siegfried.eigler@fu-berlin.de](mailto:siegfried.eigler@fu-berlin.de)

## Authors

Qing Cao – Institute of Chemistry and Biochemistry, Freie Universität Berlin, 14195 Berlin, Germany; [orcid.org/0000-0001-5691-5427](https://orcid.org/0000-0001-5691-5427)

Mira Kreßler – Department of Physics, Freie Universität Berlin, 14195 Berlin, Germany

Marleen Hußmann – Institute of Chemistry and Biochemistry, Freie Universität Berlin, 14195 Berlin, Germany

Yalei Hu – Institute of Chemistry and Biochemistry, Freie Universität Berlin, 14195 Berlin, Germany; [orcid.org/0000-0001-6708-944X](https://orcid.org/0000-0001-6708-944X)

Patryk Kusch – Department of Physics, Freie Universität Berlin, 14195 Berlin, Germany; [orcid.org/0000-0001-9180-786X](https://orcid.org/0000-0001-9180-786X)

Complete contact information is available at:

<https://pubs.acs.org/doi/10.1021/acs.chemmater.3c03166>

## Author Contributions

Q. C. performed the experiments and wrote the manuscript. M. K. and P. K. performed the KPFM and s-SNOM measurement. M. H. and Y. H. provided help and suggestions on projects. S. E. supervised the project. All authors discussed the results and commented on the manuscript.

## Notes

The authors declare no competing financial interest.

## ■ ACKNOWLEDGMENTS

This research was supported by the China Scholarship Council (CSC).

## ■ REFERENCES

- (1) Duan, X.; Wang, C.; Pan, A.; Yu, R.; Duan, X. Two-Dimensional Transition Metal Dichalcogenides as Atomically Thin Semiconductors: Opportunities and Challenges. *Chem. Soc. Rev.* **2015**, *44*, 8859–8876.
- (2) Yu, S.; Wu, X.; Wang, Y.; Guo, X.; Tong, L. 2D Materials for Optical Modulation: Challenges and Opportunities. *Adv. Mater.* **2017**, *29*, 1606128.
- (3) Moses Badlyan, N.; Pettinger, N.; Enderlein, N.; Gillen, R.; Chen, X.; Zhang, W.; Knirsch, K. C.; Hirsch, A.; Maultzsch, J. Oxidation and Phase Transition in Covalently Functionalized MoS<sub>2</sub>. *Phys. Rev. B* **2022**, *106*, 104103.
- (4) Splendiani, A.; Sun, L.; Zhang, Y.; Li, T.; Kim, J.; Chim, C. Y.; Galli, G.; Wang, F. Emerging Photoluminescence in Monolayer MoS<sub>2</sub>. *Nano Lett.* **2010**, *10*, 1271–1275.
- (5) Mak, K. F.; Lee, C.; Hone, J.; Shan, J.; Heinz, T. F. Atomically Thin MoS<sub>2</sub>: a New Direct-Gap Semiconductor. *Phys. Rev. Lett.* **2010**, *105*, 136805.
- (6) Mouri, S.; Miyauchi, Y.; Matsuda, K. Tunable Photoluminescence of Monolayer MoS<sub>2</sub> via Chemical Doping. *Nano Lett.* **2013**, *13*, 5944–5948.
- (7) Ross, J. S.; Wu, S.; Yu, H.; Ghimire, N. J.; Jones, A. M.; Aivazian, G.; Yan, J.; Mandrus, D. G.; Xiao, D.; Yao, W.; Xu, X. Electrical Control of Neutral and Charged Excitons in a Monolayer Semiconductor. *Nat. Commun.* **2013**, *4*, 1474.
- (8) Mak, K. F.; He, K.; Lee, C.; Lee, G. H.; Hone, J.; Heinz, T. F.; Shan, J. Tightly Bound Trions in Monolayer MoS<sub>2</sub>. *Nat. Mater.* **2013**, *12*, 207–211.
- (9) Nan, H.; Wang, Z.; Wang, W.; Liang, Z.; Lu, Y.; Chen, Q.; He, D.; Tan, P.; Miao, F.; Wang, X.; Wang, J.; Ni, Z. Strong Photoluminescence Enhancement of MoS<sub>2</sub> through Defect Engineering and Oxygen Bonding. *ACS Nano* **2014**, *8*, 5738–5745.
- (10) Chen, X.; Kohring, M.; Assebban, M.; Tywoniuk, B.; Bartlam, C.; Moses Badlyan, N.; Maultzsch, J.; Duesberg, G. S.; Weber, H. B.; Knirsch, K. C.; Hirsch, A. Covalent Patterning of 2D MoS<sub>2</sub>. *Chem.—Eur. J.* **2021**, *27*, 13117–13122.
- (11) Chen, X.; Assebban, M.; Kohring, M.; Bao, L.; Weber, H. B.; Knirsch, K. C.; Hirsch, A. Laser-Triggered Bottom-Up Transcription of Chemical Information: Toward Patterned Graphene/MoS<sub>2</sub> Heterostructures. *J. Am. Chem. Soc.* **2022**, *144*, 9645–9650.
- (12) Kang, N.; Paudel, H. P.; Leuenberger, M. N.; Tetard, L.; Khondaker, S. I. Photoluminescence Quenching in Single-Layer MoS<sub>2</sub> via Oxygen Plasma Treatment. *J. Phys. Chem. C* **2014**, *118*, 21258–21263.
- (13) Buscema, M.; Steele, G. A.; van der Zant, H. S. J.; Castellanos-Gomez, A. The Effect of the Substrate on the Raman and Photoluminescence Emission of Single-Layer MoS<sub>2</sub>. *Nano Res.* **2014**, *7*, 561–571.
- (14) Fang, H.; Battaglia, C.; Carraro, C.; Nemsak, S.; Ozdol, B.; Kang, J. S.; Bechtel, H. A.; Desai, S. B.; Kronast, F.; Unal, A. A.; Conti, G.; Conlon, C.; Palsson, G. K.; Martin, M. C.; Minor, A. M.; Fadley, C. S.; Yablonovitch, E.; Maboudian, R.; Javey, A. Strong Interlayer Coupling in van der Waals Heterostructures Built from Single-Layer Chalcogenides. *Proc. Natl. Acad. Sci. U.S.A.* **2014**, *111*, 6198–6202.
- (15) Novoselov, K. S.; Geim, A. K.; Morozov, S. V.; Jiang, D.; Zhang, Y.; Dubonos, S. V.; Grigorieva, I. V.; Firsov, A. A. Electric Field Effect in Atomically Thin Carbon Films. *Science* **2004**, *306*, 666–669.
- (16) Wassei, J. K.; Kaner, R. B. Graphene, a Promising Transparent Conductor. *Mater. Today* **2010**, *13*, 52–59.
- (17) Hu, Z.; Zhao, Y.; Zou, W.; Lu, Q.; Liao, J.; Li, F.; Shang, M.; Lin, L.; Liu, Z. Doping of Graphene Films: Open the way to Applications in Electronics and Optoelectronics. *Adv. Funct. Mater.* **2022**, *32*, 2203179.
- (18) Yang, M.; Wang, L.; Hu, G.; Chen, X.; Gong, P. L.; Cong, X.; Liu, Y.; Yang, Y.; Li, X.; Zhao, X.; Liu, X. Optical Identification of Interlayer Coupling of Graphene/MoS<sub>2</sub> van der Waals Heterostructures. *Nano Res.* **2021**, *14*, 2241–2246.

- (19) Li, Y.; Xu, C.-Y.; Qin, J.-K.; Feng, W.; Wang, J.-Y.; Zhang, S.; Ma, L.-P.; Cao, J.; Hu, P. A.; Ren, W.; Zhen, L. Tuning the Excitonic States in MoS<sub>2</sub>/Graphene van der Waals Heterostructures via Electrochemical Gating. *Adv. Funct. Mater.* **2016**, *26*, 293–302.
- (20) Shih, C. J.; Wang, Q. H.; Son, Y.; Jin, Z.; Blankschtein, D.; Strano, M. S. Tuning On-Off Current Ratio and Field-Effect Mobility in a MoS<sub>2</sub>-Graphene Heterostructure via Schottky Barrier Modulation. *ACS Nano* **2014**, *8*, 5790–5798.
- (21) Oh, H. M.; Jeong, H.; Han, G. H.; Kim, H.; Kim, J. H.; Lee, S. Y.; Jeong, S. Y.; Jeong, S.; Park, D. J.; Kim, K. K.; Lee, Y. H.; Jeong, M. S. Modulating Electronic Properties of Monolayer MoS<sub>2</sub> via Electron-Withdrawing Functional Groups of Graphene Oxide. *ACS Nano* **2016**, *10*, 10446–10453.
- (22) Wang, Z.; Cao, Q.; Sotthewes, K.; Hu, Y.; Shin, H. S.; Eigler, S. Interlayer Electron Modulation in van der Waals Heterostructures Assembled by Stacking Monolayer MoS<sub>2</sub> onto Monolayer Graphene with Different Electron Transfer Ability. *Nanoscale* **2021**, *13*, 15464–15470.
- (23) Wang, Y.; Neumann, C.; Hußmann, M.; Cao, Q.; Hu, Y.; Garrity, O.; Kusch, P.; Turchanin, A.; Eigler, S. Synthesis of Wet-Chemically Prepared Porous-Graphene Single Layers on Si/SiO<sub>2</sub> Substrate Increasing the Photoluminescence of MoS<sub>2</sub> in Heterostructures. *Adv. Mater. Interfaces* **2021**, *8*, 2100783.
- (24) Rao, R.; Islam, A. E.; Singh, S.; Berry, R.; Kawakami, R. K.; Maruyama, B.; Katoch, J. Spectroscopic Evaluation of Charge-Transfer Doping and Strain in Graphene/MoS<sub>2</sub> Heterostructures. *Phys. Rev. B* **2019**, *99*, 195401.
- (25) Ni, Z. H.; Wang, H. M.; Luo, Z. Q.; Wang, Y. Y.; Yu, T.; Wu, Y. H.; Shen, Z. X. The Effect of Vacuum Annealing on Graphene. *J. Raman Spectrosc.* **2010**, *41*, 479–483.
- (26) Man, M. K. L.; Deckoff-Jones, S.; Winchester, A.; Shi, G.; Gupta, G.; Mohite, A. D.; Kar, S.; Kioupakis, E.; Talapatra, S.; Dani, K. M. Protecting the Properties of Monolayer MoS<sub>2</sub> on Silicon Based Substrates with An Atomically Thin Buffer. *Sci. Rep.* **2016**, *6*, 20890.
- (27) Liu, H.; Ryu, S.; Chen, Z.; Steigerwald, M. L.; Nuckolls, C.; Brus, L. E. Photochemical Reactivity of Graphene. *J. Am. Chem. Soc.* **2009**, *131*, 17099–17101.
- (28) Kariuki, J. K.; McDermott, M. T. Nucleation and Growth of Functionalized Aryl Films on Graphite Electrodes. *Langmuir* **1999**, *15*, 6534–6540.
- (29) Tahara, K.; Kubo, Y.; Lindner, B.; Hashimoto, S.; Hirose, S.; Brown, A.; Hirsch, B.; Daukiya, L.; De Feyter, S.; Tobe, Y. Steric and Electronic Effects of Electrochemically Generated Aryl Radicals on Grafting of the Graphite Surface. *Langmuir* **2019**, *35*, 2089–2098.
- (30) Vecera, P.; Eigler, S.; Kolešnik-Gray, M.; Krstić, V.; Vierck, A.; Maultzsch, J.; Schäfer, R. A.; Hauke, F.; Hirsch, A. Degree of Functionalisation Dependence of Individual Raman Intensities in Covalent Graphene Derivatives. *Sci. Rep.* **2017**, *7*, 45165.
- (31) Kim, Y.; Herlinger, P.; Taniguchi, T.; Watanabe, K.; Smet, J. H. Reliable Postprocessing Improvement of van der Waals Heterostructures. *ACS Nano* **2019**, *13*, 14182–14190.
- (32) Illarionov, Y. Y.; Rzepa, G.; Waltl, M.; Knobloch, T.; Grill, A.; Furchi, M. M.; Mueller, T.; Grasser, T. The Role of Charge Trapping in MoS<sub>2</sub>/SiO<sub>2</sub> and MoS<sub>2</sub>/hBN Field-Effect Transistors. *2D Mater.* **2016**, *3*, 035004.
- (33) Hong, S.; Fu, D.; Hou, J.; Zhou, D.; Wang, B.; Sun, Y.; Liu, P.; Liu, K. Robust Photoluminescence Energy of MoS<sub>2</sub>/Graphene Heterostructure Against Electron Irradiation. *Sci. China Mater.* **2018**, *61*, 1351–1359.
- (34) Naumov, A.; Grote, F.; Overgaard, M.; Roth, A.; Halbig, C. E.; Nørgaard, K.; Guldi, D. M.; Eigler, S. Graphene Oxide: a One- versus Two-Component Material. *J. Am. Chem. Soc.* **2016**, *138*, 11445–11448.
- (35) Gao, W.; Alemany, L. B.; Ci, L.; Ajayan, P. M. New Insights into the Structure and Reduction of Graphite Oxide. *Nat. Chem.* **2009**, *1*, 403–408.
- (36) Garrity, O.; Rodriguez, A.; Mueller, N. S.; Frank, O.; Kusch, P. Probing the Local Dielectric Function of WS<sub>2</sub> on an Au Substrate by Near Field Optical Microscopy Operating in the Visible Spectral Range. *Appl. Surf. Sci.* **2022**, *574*, 151672.
- (37) Al-Fogra, S.; Yang, B.; Jurkiewicz, L.; Hauke, F.; Hirsch, A.; Wei, T. Spatially Resolved Janus Patterning of Graphene by Direct Laser Writing. *J. Am. Chem. Soc.* **2022**, *144*, 19825–19831.
- (38) Bao, L.; Zhao, B.; Yang, B.; Halik, M.; Hauke, F.; Hirsch, A. Hypervalent Iodine Compounds as Versatile Reagents for Extremely Efficient and Reversible Patterning of Graphene with Nanoscale Precision. *Adv. Mater.* **2021**, *33*, No. e2101653.
- (39) Hußmann, M.; Weintrub, B.; Feicht, P.; Germer, G.; Kirchhof, J. N.; Bolotin, K. I.; Eigler, S. Controlled Assembly of Artificial 2D Materials Based on the Transfer of Oxo-Functionalized Graphene. *Nanoscale Adv.* **2020**, *2*, 176–181.